Article

Fe$_3$O$_4$ Nanoparticle-Decorated Graphene Oxide Nanosheets for Magnetic Assembly of Artificial Nacre

Yang Wang, Xiang Chen, Zheng Zhang, Ting Li, Xuhui Zhang, Bihua Xia, Mingqing Chen, Tianxi Liu, and Weifu Dong*

Cite This: *ACS Appl. Nano Mater.* 2021, 4, 9689−9696

Read Online

ACCESS | Metrics & More | Article Recommendations | Supporting Information

ABSTRACT: Natural nacre, often referred as nature's armor, has a typical "brick-and-mortar" hierarchical micro-/nanoscale multilayer microstructure and remarkable tensile strength and toughness. The highly ordered multilayer microstructure of nacre provides valuable insights into constructing advanced nanocomposites. Although significant success has been achieved in simulating artificial nacre-mimetic materials on a laboratory scale, it is still difficult to apply on a large scale because of time-consuming sequential depositions. In this study, a rapid and large-scalable magnetic assembly process for the fabrication of the graphene oxide (GO)-based composite film that mimics the structure of nacre was reported. Magnetic GO nanosheets were synthesized by decorating Fe$_3$O$_4$ nanoparticles on the surface of GO nanosheets and then assembled with poly(vinyl alcohol) (PVA) solution to form nacre-mimetic nanocomposites *via* the magnetic assembly technique. The tensile strength and toughness of the MGO−PVA film can reach 248.0 ± 6.7 MPa and 7.0 ± 0.5 MJ·m^{-3}, which are 5.0 and 4.0 times higher than the pure MGO film, respectively. More interestingly, after *in situ* reduction by hydroiodic acid, the tensile strength reached as high as 340.0 ± 6.2 MPa. This work offers a rapid process of fabricating strong integration nacre-inspired materials, which shows applications in engineering, aerospace, flexible energy devices, and electromagnetic interference shielding materials.

KEYWORDS: *nacre, magnetic assembly, graphene oxide, nanocomposites, mechanical properties*
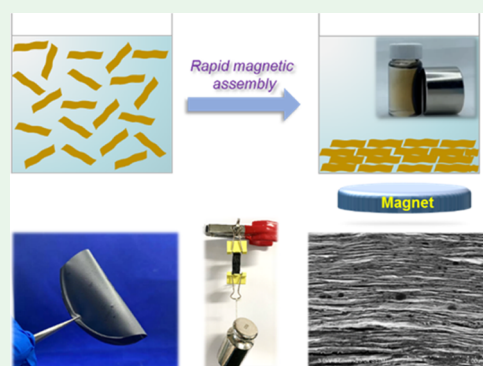
■ INTRODUCTION

With the rapid development of nanoscience and nano-technology, various nanocomposites have been prepared for engineering fields. Biological structural materials engineering influences the design of advanced functional materials in many scientific fields, from interfacial property to optical and mechanical materials.[1,2] Many natural materials possess synergistic mechanical properties by building intrinsic hierarchical structures, ranging from nano-/microscopic to macroscopic scales. Nacre, bone, and teeth are famous examples. These natural biocomposites usually contain a large number of ordered reinforcement components and a small loading of the energy-dissipating soft material. The hard/soft interface effect offers the materials excellent antifatigue properties.[3−5]

Biological nanocomposites are different from the common engineering material in concept due to their high content of the reinforcing phase. In particular, pearl oyster nacre is an organic−inorganic composites produced by some mollusks that act as an armor against external shocks; it is well known for its good strength, hardness, and toughness due to its hierarchical layered structure and sophisticated interfacial design, which are superior to many other structural materials. Nacre, with 95 vol % brittle polycrystalline aragonite (CaCO$_3$)

building blocks and 5 vol % protein, exhibits high-level combination of tensile strength and fracture toughness, which is 3 orders of magnitude higher than that of its constituents in energy terms.[6−10] It achieves a stiffness threefold higher than that of bone while having the same toughness. In order to simulate the solid structure of nacre, two-dimensional materials, such as flat double-walled carbon nanotubes,[11] montmorillonite,[12] GO,[13−18] layered double hydroxides,[19] boron nitride nanosheets,[20,21] and MXene,[22,23] have been chosen as reinforcing bricks. Energy-dissipating soft polymer matrices (such as PVA,[24] chitosan,[25] protein,[26] cellulose derivatives,[27] *etc.*) have been widely used as "mortars". The high mechanical performance mainly originates from the orderly micro-/nanoscale brick-and-mortar architecture and abundant interfacial interactions, which dictates the control-lable sliding of the brick over a large scale along with ductile stretching of the polymer.
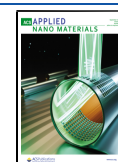
Recently, a series of techniques have been applied to fabricate nanocomposites with the brick-and-mortar architecture, including layer-by-layer (LBL) deposition, evaporation, filtration, and freeze casting.[28−31] The LBL assembly of ceramic sheets (*e.g.*, clays and alumina) and polymers has proven to be an effective method to create enhanced nanocomposites with alignment structures. For example, Brinker *et al.* reported a novel assembly method to prepare nanolayered coatings that mimic the nacre through a simple dip-coating method.[32] Aubin-Tam *et al.* reported self-assembled, nacre-mimetic composites composed of *γ*-poly-(glutamic acid), graphene oxide, and divalent cations *via* slow solvent evaporation at room temperature.[33] LBL has shown many advantages in the manufacture of nanolayered and multifunctional composite films with adjustable size, composition, and structure. These composite films exhibit excellent optical, electrical, chemical, and mechanical properties. Note that many LBL operations usually need time to achieve atomistic relaxation at the interfaces. The construction of layered films having thermodynamic equilibrium is a relative time-consuming process. Nacre-mimetic composites have also been obtained through the vacuum-assisted self-assembly process and evaporation.[34] During the evaporation of the solution, the nanoplates tend to arrange in a low energy structure, resulting in an orderly nacre-mimetic structure. Das *et al.* prepared montmorillonite−sodium carboxymethyl cellulose composite materials that are nacre-mimetic meso-structured through evaporation.[35] The obtained composite films possess outstanding mechanical preference. However, it often needs more time for solvent removal.

The ice templating is a new technique used in the fabrication of nacre-inspired composite materials, especially for controlling the micro-/nanoscale layered structure, including the bridge between the stratified layers of the scaffold and the interface interaction between the scaffold and the permeable matrix. By freezing a suspension of plates, the ice crystals *in situ* grow directionally, through the suspension, repelling and condensing the plates to self-assembly present in the suspension. After that, the ice crystals can be easily removed by thawing and drying. Deville *et al.* first took advantage of ice crystal growth as a driving force for the assembly of anisotropic particles (platelets) to form layered-hybrid materials.[36] Although the ice-templating approach is essential for the successful preparation of nacre-inspired composite materials, it still remains a challenge to reproduce the precise lamellar structure of nacre. For instance, the materials contain relatively low inorganic content and need a sintering process.

Although the great progress has been obtained in the formation of nacre composite materials, it is still very difficult to identify rapid and efficient assembly approaches to mimic strong integrated artificial nacre materials for large-scale applications in a wide range of fields. In this work, we reported a simple and rapid strategy for preparing the integrated high-performance polymer nanocomposites with a hierarchical "brick-and-mortar" structure based on the assembly of magnetic GO nanosheets. GO-magnetic sheets were prepared by attaching Fe_3O_4 to GO. PVA was chosen as the "mortar" for its large amount of hydrogen bonding. The rapid enrichment of high-concentration GO in the PVA solution is achieved by applying an external magnetic field, and the solvent is quickly removed while ensuring the assembly of the nanosheets. The magnetic assembly process resulted in MGO−PVA composites with a hierarchically ordered

inorganic−organic "brick-and-mortar" structure. These artificial nacre composite materials integrate tensile strength and toughness, exhibiting possible applications in soft electronics, engineering, aerospace, and electromagnetic interference-shielding materials.

■ EXPERIMENTAL SECTION

Materials. Graphite powder (99.9 wt % purity) was received from Qingdao Jinrilai Co., Ltd. Ferric chloride hexahydrate ($FeCl_3 \cdot 6H_2O$, 97 wt %), iron(II) sulfate heptahydrate ($FeSO_4 \cdot 7H_2O$, 99 wt %), hydroiodic (HI) acid (57 wt %), and poly(vinyl alcohol) (PVA-1799) were purchased from Aladdin-reagent Inc.

Synthesis of Magnetic GO. GO was synthesized from graphite flakes by a modified Hummers method reported previously.[37] GO was dispersed in deionized water under sonication. $FeCl_3 \cdot 6H_2O$ and $FeSO_4 \cdot 7H_2O$ (conditions: the mass feed ratio of Fe^{3+} to Fe^{2+} is 2 and the mass feed ratio of ferric ion to GO is 1) solutions were added dropwise into GO dispersion under N_2 protection and continuously stirred. $NH_3 \cdot H_2O$ solution was added slowly into the mixture to adjust the pH to 11. The final product was separated by centrifugation and washed with ethanol.

Preparation of the Nacre-Bioinspired Composite Film. The obtained magnetic GO (MGO) was dispersed into PVA aqueous solution (3 wt %) with different concentrations. The uniform suspensions of MGO in polymer solution were made by sonication. The mixed MGO−PVA solution was rapid magnetic assembled to form a MGO−PVA composite film under an external static magnetic field. Then, the excess water was removed. After being air-dried at ambient temperature, the composite films were dried in an oven at 80 °C overnight. The MGO−PVA composite film was immersed into 57 wt % HI solution in a sealed cuvette that was placed in an oil bath (70 °C, 4 h). After reduction, the composite film was washed with ethanol. The reduced MGO−PVA film was obtained after drying in a vacuum oven at 80 °C overnight.

Characterization. X-ray diffractometer (XRD) patterns were recorded using a XRD analyzer (Bruker-D8, Germany). Fourier transform infrared (FTIR) data were obtained on a Fourier transform infrared spectrometer (Nicolet 6700, Thermo Scientific, USA). Thickness of the nanosheets was examined by an atomic force microscope (AFM MuLtimode 8, Bruker Nano, U.S.A.). The morphology of the scaffolds and nanocomposites was observed by a scanning electron microscope (Hitachi S-4800). The accelerating voltage was increased up to 15 kV for energy-dispersive X-ray spectroscopy (EDX) measurements. Thermogravimetric analysis (TGA) was carried out on PerkinElmer with a heating rate of 10 °C min⁻¹. The hysteresis loop of the composite film in the range of −20 to 20 kOe is obtained by VSM analysis (LakeShore 7404). The tensile tests were carried out with an Instron 5967 tester at a strain rate of 1 mm·min⁻¹. Mechanical properties were characterized under ambient conditions (25 °C, 15% RH). All of the samples were cut into strips with the width of 5 mm and length of 30 mm. Toughness (*W*) is the energy dissipation of the composites before fracture, calculated by eq 1

$$W = \int_0^{\varepsilon_f} \sigma \, d\varepsilon \tag{1}$$

where σ and ε is the stress and strain and ε_f is the failure strain, respectively.

■ RESULTS AND DISCUSSION

Figure 1 shows the strategy for the rapid magnetic assembly process of MGO−PVA composites. First, GO was synthesized from graphite powder *via* the improved Hummer's method. GO nanosheets was modified with Fe_3O_4 nanoparticles. The obtained MGO was blended with PVA solution. Then, the mixture was rapid magnetic assembled to form the MGO−
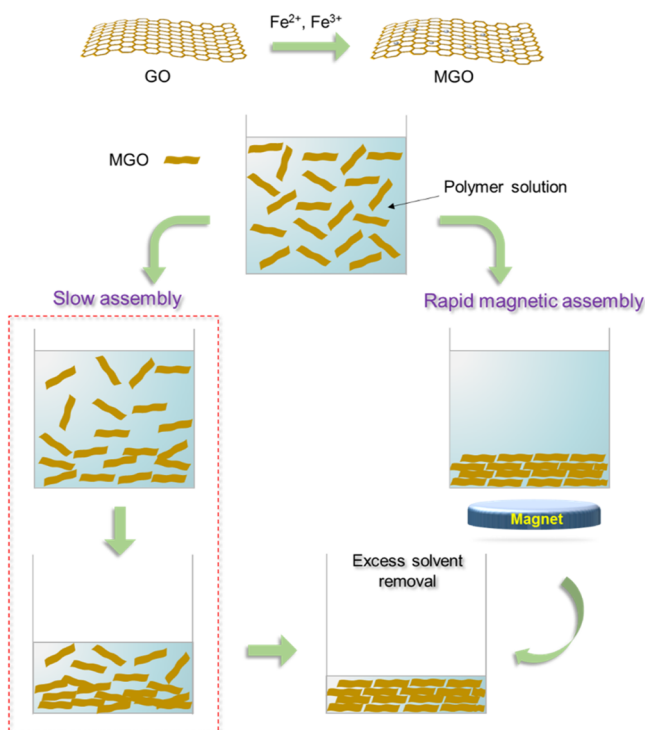
Figure 1. Illustration of the rapid self-assembly process of MGO–PVA composite films.

PVA composite film by applying an external static magnetic field.

The chemical compositions of GO, Fe_3O_4 and MGO were examined by XRD. As shown in Figure 2a, for GO, an obvious diffraction peak is attributed to the diffraction index of (001). Typical XRD pattern peaks of Fe_3O_4 are observed in MGO at 2θ of 30.1, 35.6, 43.1, 53.6, 57.0, and 62.7° corresponding to (220), (311), (400), (422), (511), and (440), respectively, which are consistent with Joint Committee on Powder Diffraction Standards (card no. 19-0629).[38] The sharp diffraction peak of 2θ = 10.6 for GO disappears after loading Fe_3O_4 nanoparticles, showing that the interlayer distance expanded.[39] The FT-IR spectra of GO, Fe_3O_4, and MGO are shown in Figure 2b. The broad band at 3326 cm^{-1} represents hydroxyl group (−OH) stretching vibration. The −C=O stretching appears at 1728 cm^{-1}, while the bands at 1622 and 1046 cm^{-1} suggest the existence of −C=C and C−O−C,

respectively.[40] In the Fe_3O_4 spectrum, the absorption peak at 578 cm^{-1} belongs to the Fe−O bond stretching vibration.[41] For the FTIR spectrum of MGO, a strong Fe−O peak at 575 cm^{-1} is observed, indicating that the GO sheets were successfully modified with Fe_3O_4 nanoparticles.

Figure 3a shows the AFM image of the GO nanosheets with lateral dimensions of several micrometers on a silicon substrate. The GO nanosheet exhibits a typical 2D microscale layer with 0.96 nm thickness, which was in agreement with single-layered GO. The AFM image of MGO nanosheets is shown in Figure 3b. The Fe_3O_4 nanoparticles with a diameter of ∼10 nm is observed on the as-obtained GO nanosheets, indicating that MGO was successfully prepared.

Figure 4a shows the TGA thermograms of samples. The weight loss process of GO can be divided into two stages. The first weight loss below 100 °C can be attributed to the removal of residual aqueous solution. The second stage shows a rapid weight loss from 150 to 200 °C corresponding to the evaporation of oxygen-containing functional groups. Fe_3O_4 has no obvious weight loss in the temperature range of 50−700 °C. The TGA curve of MGO clearly shows that the stages of decomposition shift to a higher temperature and exhibit thermal stability due to the existence of Fe_3O_4 nanoparticles. PVA undergoes a large amount of thermal decomposition in the high temperature area (500−700 °C). The weight loss of MGO−PVA composite films decreases with the amount of PVA. According to the TGA curves, the amount of Fe_3O_4 in MGO and PVA in the composite film can be calculated. The experimental Fe_3O_4 content in MGO is about 16.4 wt %. The contents of PVA in MGO−PVA composite films are about 4.8, 13.2, 18.8, and 29.3 wt %.

The magnetic property of the composite film was investigated using VSM. The magnetization saturation value of MGO−PVA *versus* the applied magnetic field from −20 to 20 kOe attains 5.5 emu·g^{-1}. As expected, an obvious decrease in the magnetic value of MGO−PVA (18.8 wt %) compared to that of pure Fe_3O_4 nanoparticles (∼70 emu·g^{-1}) is attributed to the nonmagnetic PVA polymer (Figure 4b), but the present saturation magnetization of MGO−PVA is still appropriate for the facile magnetic assembly process of artificial nacre composite films. Under an external magnetic field, the MGO−PVA mixture has a rapid response within ∼60 s (Figure 4c).

The cross-sectional morphologies of the pure MGO and MGO−PVA composite film were observed by SEM (Figure 5). All the films exhibit a highly ordered "brick-and-mortar"
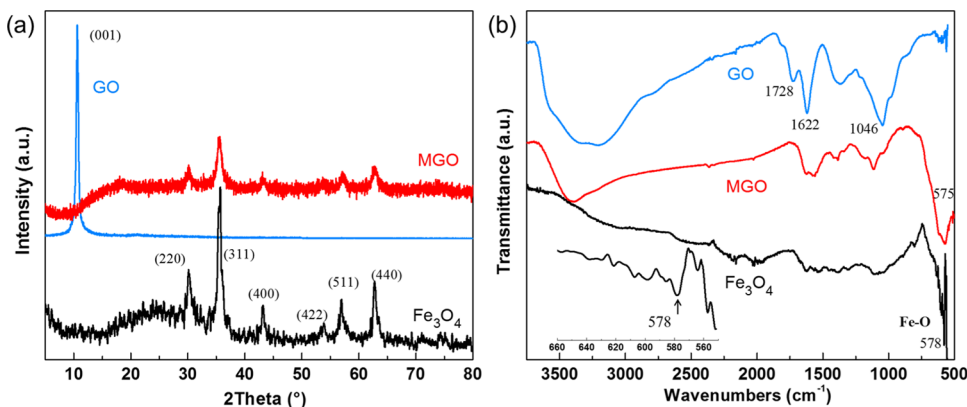
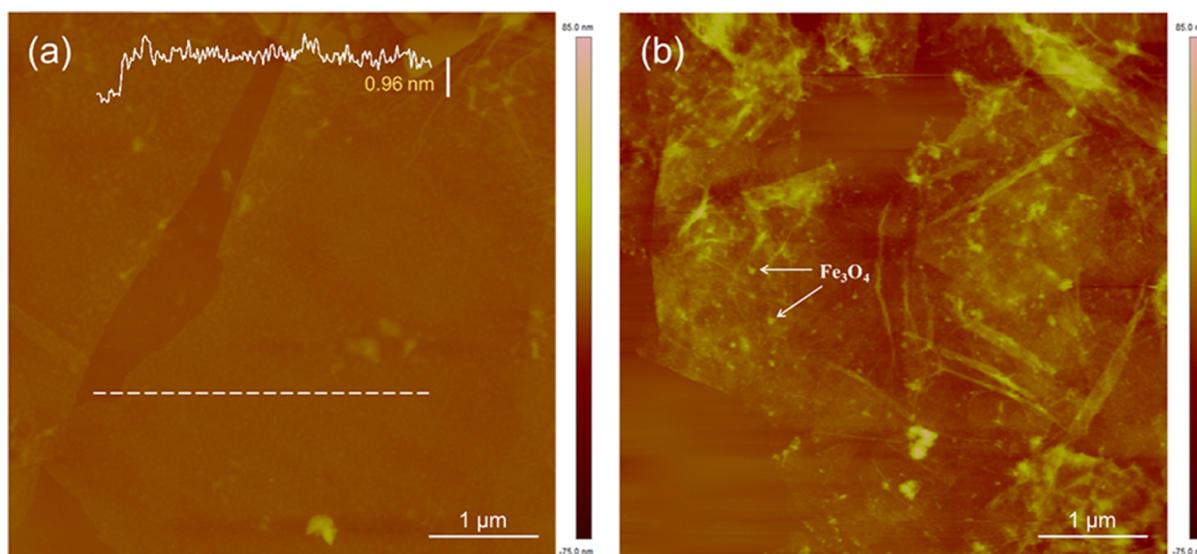**Figure 2.** (a) XRD patterns and (b) FTIR of the pure GO, Fe_3O_4, and MGO, respectively.
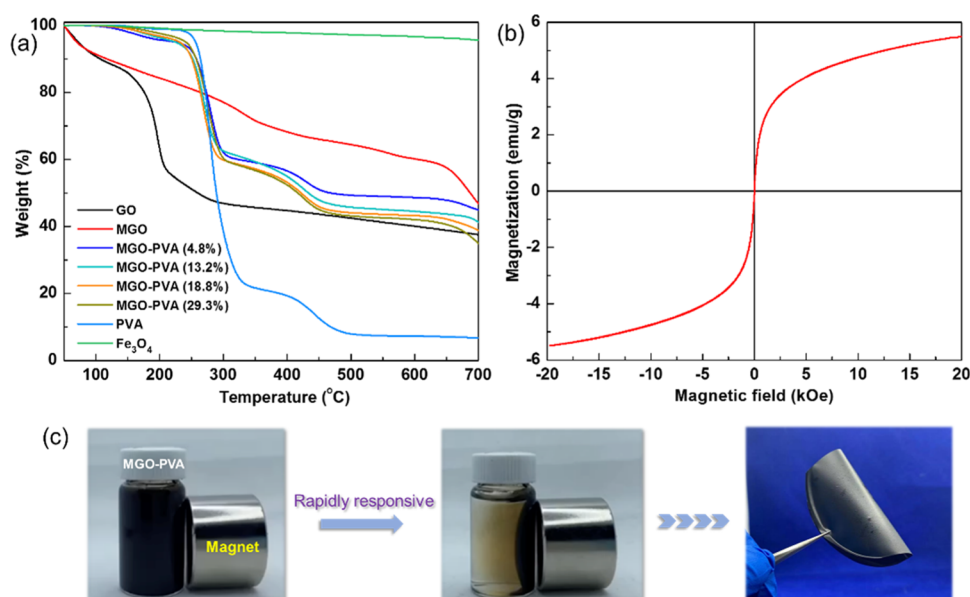
Figure 3. AFM image of (a) GO and (b) MGO nanosheets.

Figure 4. (a) TGA curves of GO, Fe_3O_4, MGO, PVA, and MGO−PVA composite films. (b) Magnetization curve of the MGO−PVA (18.8 wt %) composite film. (c) Rapid magnetic assembly of the MGO−PVA mixture (digital image of the folded MGO−PVA prepared by a magnetic assembly process, confirming the flexibility of the composite film).
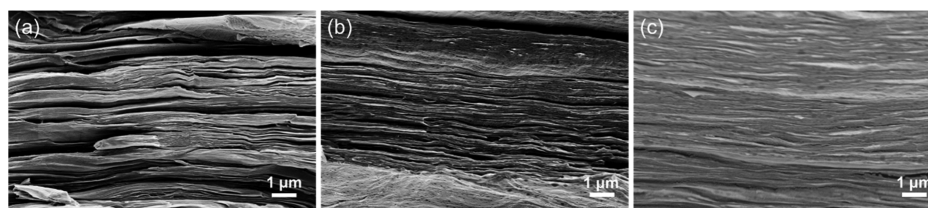

Figure 5. SEM cross-sectional images of (a) pure MGO, (b) MGO−PVA (4.8 wt %), and (c) MGO−PVA (18.8 wt %) composite films.

architecture similar to that of nacre. The pure MGO film presents prominent interlayer gaps with withdrawn nanosheets, indicating the weak interface interaction. MGO in the MGO−PVA composite film is widely oriented horizontally. As the PVA polymer content increases, the sharp contours of the MGO nanosheets are visibly piled close together and the gaps between adjacent MGO sheets become inconspicuous due to

the increased loading of PVA wrapping the MGO sheets. The elemental mapping was further performed to investigate the fractured surfaces of the nanocomposite films, indicating that Fe_3O_4 is uniformly distributed between the adjacent MGO nanosheets (Figure 6). The results also provided another evidence of the introduction of Fe_3O_4 into the surface of GO.
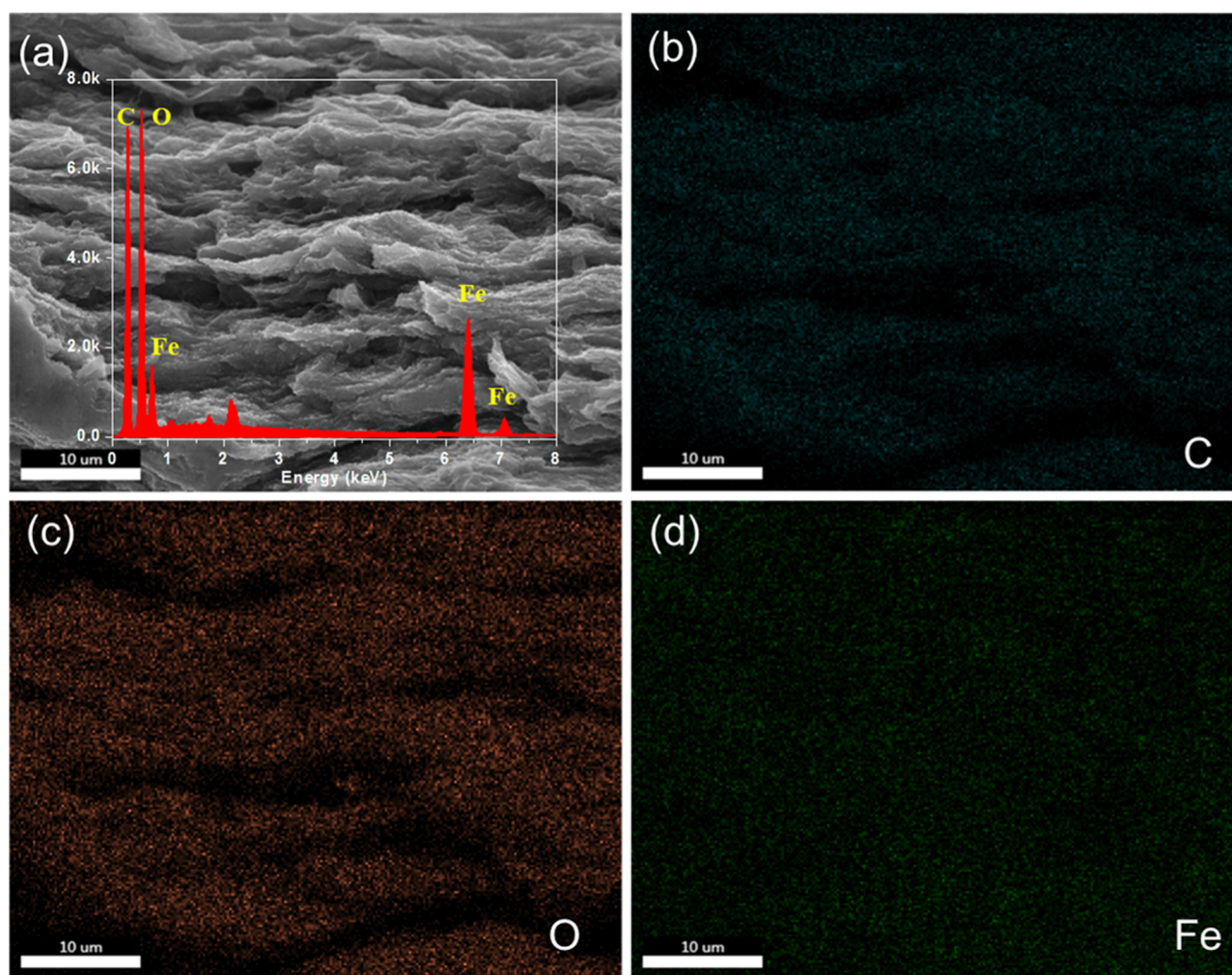
Figure 6. (a) SEM mapping photograph of fracture surfaces of the composite film and elemental mapping images of the composite film: C mapping (b), O mapping (c), and Fe mapping (d).

To further investigate the interface interaction of composite films, stress−strain curves of the prepared samples are shown in Figure 7a. The mechanical properties of all the composites were evaluated, as shown in Figure 7b, and the detailed data are listed in Table 1. The pure MGO film exhibits a tensile strength of 50.0 ± 3.7 MPa, a fracture strain of 2.1 ± 0.3%, a Young's modulus of 1.8 ± 0.2 GPa, and a toughness of 0.5 ± 0.1 MJ·m^{-3}. It is noted that the mechanical properties can be significantly improved with the addition of PVA. By increasing the PVA content to 13.2 wt %, the tensile strength and toughness of the composite film increases to 152.0 ± 2.5 MPa and 3.2 ± 0.4 MJ·m^{-3}, respectively (curve III). The maximum tensile strength, toughness, and Young's modulus of the resultant nanocomposite film are improved to 248.0 ± 6.7 MPa, 7.0 ± 0.5 MJ·m^{-3}, and 7.2 ± 0.4 GPa, respectively (curve IV), which are attributed to the introduction of intermolecular hydrogen bonding between the hydroxyl groups of the PVA polymer and MGO nanosheets. With the further addition of PVA, the tensile strength and Young's modulus decrease. This may be attributed to the fact that the excessive PVA polymer cannot connect the MGO nanosheets effectively. PVA chains may also increase the interlayer spacing of the composite films, resulting in a decrease in compactness. Despite this, the composite film retains its high mechanical strength and toughness.

To clarify the synergistic effect of composite films, a fracture model is proposed in Figure 7c. It is well known that when tensile strain is gradually applied to the MGO film, relatively adjacent building plates begin to slip until cracks appear under large external strain, which leads to tensile failure. For MGO−PVA composite films, at the initial loading stage, the MGO slide, the weaker hydrogen bonds between MGO and PVA broke at first, and then, the spiral PVA long chain is stretched, leading to energy dissipation. When stretching continues, the stronger hydrogen bonds on the interface are disrupted and more energy is absorbed, causing the pulling out of MGO nanosheets. As the bridges cracked, the composite films finally destruct. Finally, MGO−PVA (18.8 wt %) was immersed into HI for in situ reduction. Interestingly, when the composite film was reduced by hydroiodic acid, the tensile strength of the reduced MGO−PVA composite film reaches to 340.0 ± 6.2 MPa, which is more than 6.8 times that of the pure MGO film. With exception of the hydrogen bonding, such a great enhancement is maybe due to strong interaction caused by *in situ* reduction. The reduced MGO also has strong van Waals forces to improve the interaction with the polymer. The reduction of interlayer spacing between adjacent MGO sheets after reduction and π-interactions between nanosheets and the polymer could also play key roles in enhancing the mechanical properties of MGO−PVA composite films.
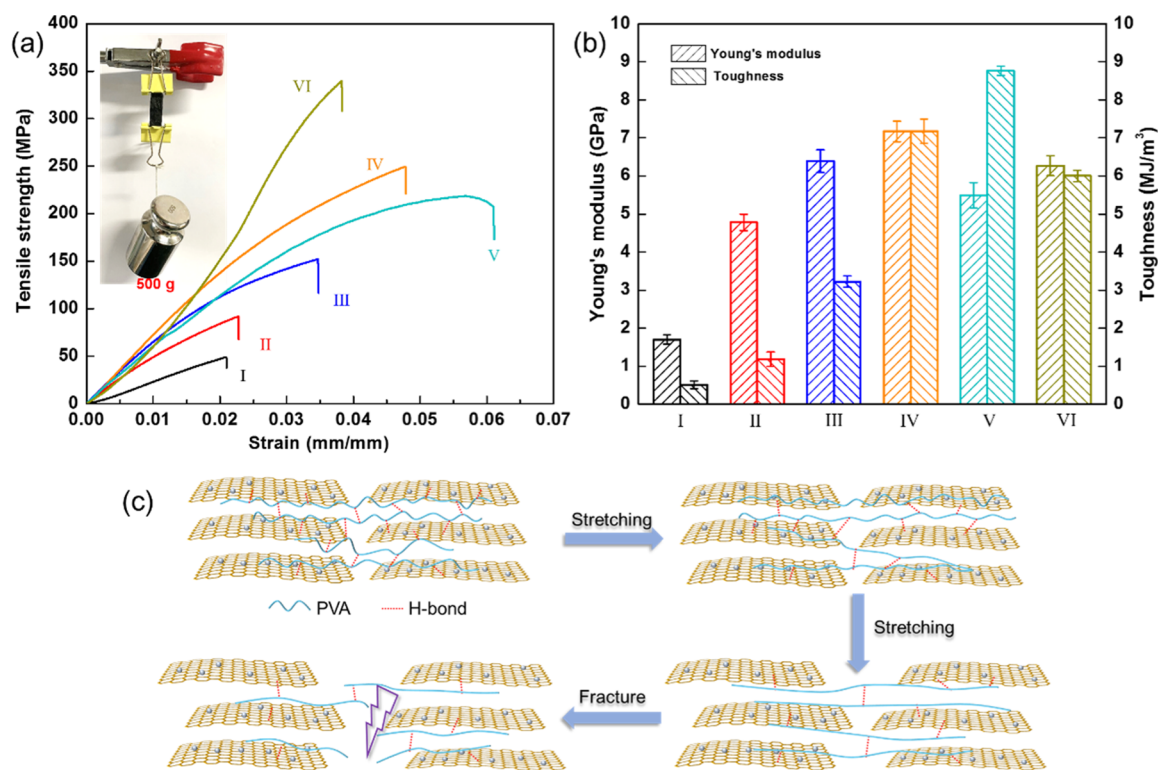
Figure 7. (a) Tensile stress−strain curves of the pure MGO film (curve I), MGO−PVA (4.8 wt %) (curve II), MGO−PVA (13.2 wt %) (curve III), MGO−PVA (18.8 wt %) (curve IV), MGO−PVA (29.3 wt %) (curve V), and reduced MGO−PVA (18.8 wt %) (curve VI) [inset: The MGO−PVA(18.8 wt %) composite film had a high tensile strength and could completely support ∼500 g of mass]. (b) Young's modulus and toughness of MGO−PVA composite films. (c) Schematic illustration of the fracture mechanism the composite films.

Table 1. Mechanical Properties of MGO, MGO−PVA, and Reduced MGO−PVA (rMGO−PVA) Composite Films

name	tensile strength (MPa)	Young's modulus (GPa)	toughness (MJ·m^{-3})
MGO	50.0 ± 3.7	1.8 ± 0.2	0.5 ± 0.1
MGO−PVA (4.8 wt %)	91.0 ± 2.6	4.8 ± 0.3	1.2 ± 0.2
MGO−PVA (13.2 wt %)	152.0 ± 2.5	6.4 ± 0.3	3.2 ± 0.4
MGO−PVA (18.8 wt %)	248.0 ± 6.7	7.2 ± 0.4	7.0 ± 0.5
MGO−PVA (29.3 wt %)	218 ± 5.5	5.5 ± 0.3	8.7 ± 0.1
rMGO−PVA (18.8 wt %)	340.0 ± 6.2	6.3 ± 0.2	6.0 ± 0.1

CONCLUSIONS

In summary, inspired by the "brick-and-mortar" structure of nacre, MGO−PVA composite films with the nacre-inspired architecture are fabricated *via* the rapid magnetic assembly. The method involves the synthesis of MGO nanosheets and magnetic assembly. Compared with the traditional vacuum-assisted assembly procedure, the magnetic assembly is faster and more efficient. The tensile strength and toughness of the MGO−PVA film can be increased to 248.0 ± 6.7 MPa and 7.0 ± 0.5 MJ·m^{-3}, which are 5.0 and 4.0 times higher than that of the pure MGO film. What is more, after *in situ* reduction by hydroiodic acid, the tensile strength value reached as high as 340.0 ± 6.2 MPa. This magnetic assembly produce provides novel perspectives for the fabrication of strong integrated materials in the application of flexible energy devices, engineering, aerospace, and electromagnetic interference shielding materials.

ASSOCIATED CONTENT

Supporting Information

The Supporting Information is available free of charge at https://pubs.acs.org/doi/10.1021/acsanm.1c02061.

Rapid magnetic assembly of the MGO−PVA mixture (MP4)

AUTHOR INFORMATION

Corresponding Author

    Weifu Dong − *The Key Laboratory of Synthetic and Biological Colloids, Ministry of Education, School of Chemical and Material Engineering, Jiangnan University, Wuxi 214122, China;* orcid.org/0000-0002-7432-8362; Phone: +86-510-8532-6290; Email: wfdong@jiangnan.edu.cn

Authors

    Yang Wang − *The Key Laboratory of Synthetic and Biological Colloids, Ministry of Education, School of Chemical and Material Engineering, Jiangnan University, Wuxi 214122, China;* orcid.org/0000-0001-7875-9111

    Xiang Chen − *The Key Laboratory of Synthetic and Biological Colloids, Ministry of Education, School of Chemical and Material Engineering, Jiangnan University, Wuxi 214122, China*

    Zheng Zhang − *The Key Laboratory of Synthetic and Biological Colloids, Ministry of Education, School of Chemical and Material Engineering, Jiangnan University, Wuxi 214122, China*

    Ting Li − *The Key Laboratory of Synthetic and Biological Colloids, Ministry of Education, School of Chemical and*

Material Engineering, Jiangnan University, Wuxi 214122, China

Xuhui Zhang − *The Key Laboratory of Synthetic and Biological Colloids, Ministry of Education, School of Chemical and Material Engineering, Jiangnan University, Wuxi 214122, China*

Bihua Xia − *The Key Laboratory of Synthetic and Biological Colloids, Ministry of Education, School of Chemical and Material Engineering, Jiangnan University, Wuxi 214122, China*

Mingqing Chen − *The Key Laboratory of Synthetic and Biological Colloids, Ministry of Education, School of Chemical and Material Engineering, Jiangnan University, Wuxi 214122, China;* ● orcid.org/0000-0002-4207-8696

Tianxi Liu − *The Key Laboratory of Synthetic and Biological Colloids, Ministry of Education, School of Chemical and Material Engineering, Jiangnan University, Wuxi 214122, China*

Complete contact information is available at:
https://pubs.acs.org/10.1021/acsanm.1c02061

Notes

The authors declare no competing financial interest.

■ REFERENCES

(1) Lossada, F.; Hoenders, D.; Guo, J.; Jiao, D.; Walther, A. Self-Assembled Bioinspired Nanocomposites. *Acc. Chem. Res.* **2020**, *53*, 2622−2635.

(2) Merindol, R.; Walther, A. Materials Learning from Life: Concepts for Active, Adaptive and Autonomous Molecular Systems. *Chem. Soc. Rev.* **2017**, *46*, 5588−5619.

(3) Lossada, F.; Jiao, D.; Hoenders, D.; Walther, A. Recyclable and Light-Adaptive Vitrimer-based Nacre-Mimetic Nanocomposites. *ACS Nano* **2021**, *15*, 5043−5055.

(4) Zhang, W.; Zheng, K.; Ren, J.; Fan, Y.; Ling, S. Strong, Ductile and Lightweight Bionanocomposites Constructed by Bioinspired Hierarchical Assembly. *Compos. Commun.* **2020**, *17*, 97−103.

(5) Wang, Y.; Liu, Q.; Lan, Z.-F.; Zhang, B.; Zhang, H.-Q.; Liu, J.-W.; Ye, F. Strong and Tough Bioinspired Nacre-Like B4C/Al Functionally Graded Materials with Eliminated Abrupt Interfaces. *Compos. Commun.* **2021**, *25*, 100741.

(6) Qiu, S.; Ren, X.; Zhou, X.; Zhang, T.; Song, L.; Hu, Y. Nacre-Inspired Black Phosphorus/Nanofibrillar Cellulose Composite Film with Enhanced Mechanical Properties and Superior Fire Resistance. *ACS Appl. Mater. Interfaces* **2020**, *12*, 36639−36651.

(7) Wan, S.; Chen, Y.; Fang, S.; Wang, S.; Xu, Z.; Jiang, L.; Baughman, R. H.; Cheng, Q. High-Strength Scalable Graphene Sheets by Freezing Stretch-Induced Alignment. *Nat. Mater.* **2021**, *20*, 624−631.

(8) Wang, Y.; Yuan, H.; Ma, P.; Bai, H.; Chen, M.; Dong, W.; Xie, Y.; Deshmukh, Y. S. Superior Performance of Artificial Nacre based on Graphene Oxide Nanosheets. *ACS Appl. Mater. Interfaces* **2017**, *9*, 4215−4222.

(9) Guan, Q.-F.; Yang, H.-B.; Yin, C.-H.; Han, Z.-M.; Yang, K.-P.; Ling, Z.-C.; Yu, S.-H. Nacre-Inspired Sustainable Coatings with

Remarkable Fire-Retardant and Energy-Saving Cooling Performance. *ACS Mater. Lett.* **2021**, *3*, 243−248.

(10) Liu, J.; Cui, T.; Ding, Y. Biomimetic Gold Nanoparticles. *Compos. Commun.* **2018**, *10*, 209−216.

(11) Cheng, Q.; Li, M.; Jiang, L.; Tang, Z. Bioinspired Layered Composites based on Flattened Double-Walled Carbon Nanotubes. *Adv. Mater.* **2012**, *24*, 1838−1843.

(12) Xu, D.; Wang, S.; Berglund, L. A.; Zhou, Q. Surface Charges Control the Structure and Properties of Layered Nanocomposite of Cellulose Nanofibrils and Clay Platelets. *ACS Appl. Mater. Interfaces* **2021**, *13*, 4463−4472.

(13) Shu, Y.; You, T.; Xing, C.; Liang, B.; Chen, H.; Yin, P. Artificial Nacre Nanocomposites based on All-Inorganic Nanoarchitectures with High Mechanical Properties and Dye Separation Performance. *Ind. Eng. Chem. Res.* **2021**, *60*, 2455−2462.

(14) Wang, Y.; Li, T.; Ma, P.; Zhang, S.; Zhang, H.; Du, M.; Xie, Y.; Chen, M.; Dong, W.; Ming, W. Artificial Nacre from Supramolecular Assembly of Graphene Oxide. *ACS Nano* **2018**, *12*, 6228−6235.

(15) Wan, S.; Jiang, L.; Cheng, Q. Design Principles of High-Performance Graphene Films: Interfaces and Alignment. *Matter* **2020**, *3*, 696−707.

(16) Sun, C.; Li, P.; Huang, H.; Ming, X.; Yang, M.; Liu, Y.; Gao, C. Plasticization Stretching Strategy Towards High Strength Nacre-Like Graphene-based Composites. *Compos. Commun.* **2021**, *27*, 100815.

(17) Liang, X.; Cheng, Q. Synergistic Reinforcing Effect from Graphene and Carbon Nanotubes. *Compos. Commun.* **2018**, *10*, 122−128.

(18) Guo, Y.; Ruan, K.; Shi, X.; Yang, X.; Gu, J. Factors Affecting Thermal Conductivities of the Polymers and Polymer Composites: A Review. *Compos. Sci. Technol.* **2020**, *193*, 108134.

(19) Shu, Y.; Yin, P.; Wang, J.; Liang, B.; Wang, H.; Guo, L. Bioinspired Nacre-Like Heparin/Layered Double Hydroxide Film with Superior Mechanical, Fire-Shielding, and UV-Blocking Properties. *Ind. Eng. Chem. Res.* **2014**, *53*, 3820−3826.

(20) Yan, Q.; Dai, W.; Gao, J.; Tan, X.; Lv, L.; Ying, J.; Lu, X.; Lu, J.; Yao, Y.; Wei, Q.; Sun, R.; Yu, J.; Jiang, N.; Chen, D.; Wong, C.-P.; Xiang, R.; Maruyama, S.; Lin, C.-T. Ultrahigh-Aspect-Ratio Boron Nitride Nanosheets Leading to Superhigh in-Plane Thermal Conductivity of Foldable Heat Spreader. *ACS Nano* **2021**, *15*, 6489−6498.

(21) Xiao, H.; Zhang, Z. P.; Huang, Z. X.; Rong, M. Z.; Zhang, M. Q. Highly Thermally Conductive, Superior Flexible and Surface Metallisable Boron Nitride Paper Fabricated by A Facile and Scalable Approach. *Compos. Commun.* **2021**, *23*, 100584.

(22) Cao, W.-T.; Chen, F.-F.; Zhu, Y.-J.; Zhang, Y.-G.; Jiang, Y.-Y.; Ma, M.-G.; Chen, F. Binary Strengthening and Toughening of MXene/Cellulose Nanofiber Composite Paper with Nacre-Inspired Structure and Superior Electromagnetic Interference Shielding Properties. *ACS Nano* **2018**, *12*, 4583−4593.

(23) Wan, S.; Li, X.; Wang, Y.; Chen, Y.; Xie, X.; Yang, R.; Tomsia, A. P.; Jiang, L.; Cheng, Q. Strong Sequentially Bridged MXene Sheets. *Proc. Natl. Acad. Sci. U.S.A.* **2020**, *117*, 27154−27161.

(24) Huang, S.; Phua, S. L.; Liu, W.; Ding, G.; Lu, X. Nacre-Like Composite Films Based on Mussel-Inspired "glue" and Nanoclay. *RSC Adv.* **2014**, *4*, 1425−1431.

(25) Wan, S.; Peng, J.; Li, Y.; Hu, H.; Jiang, L.; Cheng, Q. Use of Synergistic Interactions to Fabricate Strong, Tough, and Conductive Artificial Nacre Based on Graphene Oxide and Chitosan. *ACS Nano* **2015**, *9*, 9830−9836.

(26) Zhao, J.; Miao, B.; Yang, P. Biomimetic Amyloid-Like Protein/Laponite Nanocomposite Thin Film through Regulating Protein Conformation. *ACS Appl. Mater. Interfaces* **2020**, *12*, 35435−35444.

(27) Sheng, N.; Chen, S.; Zhang, M.; Wu, Z.; Liang, Q.; Ji, P.; Wang, H. TEMPO-Oxidized Bacterial Cellulose Nanofibers/Graphene Oxide Fibers for Osmotic Energy Conversion. *ACS Appl. Mater. Interfaces* **2021**, *13*, 22416−22425.

(28) Zhao, N.; Yang, M.; Zhao, Q.; Gao, W.; Xie, T.; Bai, H. Superstretchable Nacre-Mimetic Graphene/Poly(vinyl alcohol) Com-

posite Film Based on Interfacial Architectural Engineering. *ACS Nano* **2017**, *11*, 4777−4784.

(29) Wang, Y.; Zhang, Z.; Li, T.; Ma, P.; Zhang, X.; Xia, B.; Chen, M.; Du, M.; Liu, T.; Dong, W. Artificial Nacre Epoxy Nanomaterials Based on Janus Graphene Oxide for Thermal Management Applications. *ACS Appl. Mater. Interfaces* **2020**, *12*, 44273−44280.

(30) Rodrigues, J. R.; Alves, N. M.; Mano, J. F. Nacre-Inspired Nanocomposites Produced Using Layer-by-Layer Assembly: Design Strategies and Biomedical Applications. *Mater. Sci. Eng., C* **2017**, *76*, 1263−1273.

(31) Cheng, Q.; Jiang, L. Mimicking Nacre by Ice Templating. *Angew. Chem., Int. Ed.* **2017**, *56*, 934−935.

(32) Sellinger, A.; Weiss, P. M.; Nguyen, A.; Lu, Y.; Assink, R. A.; Gong, W.; Brinker, C. J. Continuous Self-Assembly of Organic−Inorganic Nanocomposite Coatings that Mimic Nacre. *Nature* **1998**, *394*, 256−260.

(33) Liang, K.; Spiesz, E. M.; Schmieden, D. T.; Xu, A.-W.; Meyer, A. S.; Aubin-Tam, M.-E. Bioproduced Polymers Self-Assemble with Graphene Oxide into Nanocomposite Films with Enhanced Mechanical Performance. *ACS Nano* **2020**, *14*, 14731−14739.

(34) Putz, K. W.; Compton, O. C.; Segar, C.; An, Z.; Nguyen, S. T.; Brinson, L. C. Evolution of Order During Vacuum-Assisted Self-Assembly of Graphene Oxide Paper and Associated Polymer Nanocomposites. *ACS Nano* **2011**, *5*, 6601−6609.

(35) Das, P.; Schipmann, S.; Malho, J.-M.; Zhu, B.; Klemradt, U.; Walther, A. Facile Access to Large-Scale, Self-Assembled, Nacre-Inspired, High-Performance Materials with Tunable Nanoscale Periodicities. *ACS Appl. Mater. Interfaces* **2013**, *5*, 3738−3747.

(36) Bouville, F.; Maire, E.; Meille, S.; Van de Moortèle, B.; Stevenson, A. J.; Deville, S. Strong, Tough and Stiff Bioinspired Ceramics from Brittle Constituents. *Nat. Mater.* **2014**, *13*, 508−514.

(37) Lian, M.; Fan, J.; Shi, Z.; Zhang, S.; Li, H.; Yin, J. Gelatin-Assisted Fabrication of Graphene-Based Nacre with High strength, Toughness, and Electrical Conductivity. *Carbon* **2015**, *89*, 279−289.

(38) Zhao, J.; Yang, B.; Zheng, Z.; Yang, J.; Yang, Z.; Zhang, P.; Ren, W.; Yan, X. Facile Preparation of One-Dimensional Wrapping Structure: Graphene Nanoscroll-Wrapped of Fe_3O_4 Nanoparticles and Its Application for Lithium-Ion Battery. *ACS Appl. Mater. Interfaces* **2014**, *6*, 9890−9896.

(39) Bai, T.; Liu, Z.; Pei, Z.; Fang, W.; Ma, Y. Tribological Performance Studies of Waterborne Polyurethane Coatings with Aligned Modified Graphene Oxide@ Fe_3O_4. *ACS Omega* **2021**, *6*, 9243−9253.

(40) Marcano, D. C.; Kosynkin, D. V.; Berlin, J. M.; Sinitskii, A.; Sun, Z.; Slesarev, A.; Alemany, L. B.; Lu, W.; Tour, J. M. Improved Synthesis of Graphene Oxide. *ACS Nano* **2010**, *4*, 4806−4814.

(41) Wan, X.; Zhan, Y.; Long, Z.; Zeng, G.; Ren, Y.; He, Y. High-performance magnetic poly (arylene ether nitrile) nanocomposites: Co-modification of Fe_3O_4 via mussel inspired poly(dopamine) and amino functionalized silane KH550. *Appl. Surf. Sci.* **2017**, *425*, 905−914.